PUBLICATIONS OF THE ASTRONOMICAL SOCIETY OF THE PACIFIC
97:183–198, February 1985

THE NEW NEAR-INFRARED ARRAY CAMERA AT THE UNIVERSITY OF ROCHESTER

WILLIAM J. FORREST, ANDREA MONETI, CHARLES E. WOODWARD, AND JUDITH L. PIPHER

University of Rochester and C. E. K. Mees Observatory, River Campus Station
Rochester, New York 14627

AND

ALAN HOFFMAN

Santa Barbara Research Center, 75 Coromar Drive, Goleta, California 93118

Received 1984 August 15, revised 1984 November 1

A new near-infrared array camera for use in the 1 μm–5 μm region of the spectrum has been constructed at the University of Rochester. This camera has been used successfully at the C. E. Kenneth Mees Observatory of the University of Rochester and at Kitt Peak National Observatory, National Optical Astronomy Observatories. The camera is based on a 32 × 32 element InSb array on loan from the Santa Barbara Research Center. The performance of most of the individual detectors is comparable to or better than the performance of any single element InSb detector system currently in use for astronomy. We give a thorough description of the camera system and of the image processing, and we present some images of various astronomical objects that are presently under investigation by our research group.

Key words: instrumentation—array detectors—IR imaging

I. Introduction

A new near-infrared array camera system has been developed at the University of Rochester for astronomical imaging in the 1 μm–5 μm spectral range. The camera uses a hybrid infrared Charge Coupled Device (IR CCD) which consists of a 32 × 32 array of InSb photodiodes bump-bonded[1] to a silicon CCD which is used for charge storage and readout. The array is on loan to the University of Rochester from the Santa Barbara Research Center (SBRC), and is not available commercially. The new array camera has been used successfully at the C. E. Kenneth Mees Observatory 0.6-m telescope and at the Kitt Peak National Observatory 1.3-m telescope.

The purpose of this paper is to give a detailed description of the instrument, its use, and its performance. A brief description of the camera system (section II) will be followed by a section on laboratory testing and system performance (section III). In section IV we will address the astronomical uses of the camera, and we will also discuss our observing technique and our method of image processing. In section V we present a few examples of astronomical images obtained with the new array camera and present measurements of the system sensitivity achieved while observing.

II. The Array Camera

The focal-plane array that is at the heart of the new camera has been described in the literature (Parrish et al. 1978; Hoendervoogt et al. 1978), and a previous description of the initial system was given by Forrest and Pipher (1983). Astronomical data obtained with the new camera have been presented at several astronomical meetings (Forrest et al. 1983; Moneti et al. 1983; Moneti 1984).

A block diagram of the complete camera system is shown in Figure 1, and a simplified schematic of the array is shown in Figure 2. The description below refers to Figure 2 (pp. 186–187).

Photons in the 1 μm-5 μm range incident on the InSb array generate electron-hole pairs which are separated by the p-n junctions causing the holes to travel into the underlying CCD through the input diffusions (direct injection); after passing through an input MOSFET the photocharge is stored underneath the V_{ST} electrodes (labeled "Storage Site" in Fig. 2a). When sufficient photocharge has been accumulated, the ϕ_{T1} transfer gates are pulsed low, and the photocharge is allowed to spill into the ϕ_{12} wells of the "SLOW MUX" CCD shift registers (Fig. 2a). After ϕ_{T1} is reset high, the charge packets are transferred by the SLOW MUX into the output shift register, the "FAST MUX" (Fig. 2a), which, in turn, shifts them to the output amplifier (Fig. 2b). The output of one CCD frame then consists of a series of 1024 pulses: each pulse height is proportional to the number of photons incident on a particular pixel of the array during the previous integration time.

Characteristics of the array are listed in Table I. There are several other features of the array which make it well suited for astronomical observations.

1. Individual "detector gates" surround each of the

[1]The diodes are electrically contacted to the silicon with bumps of indium.

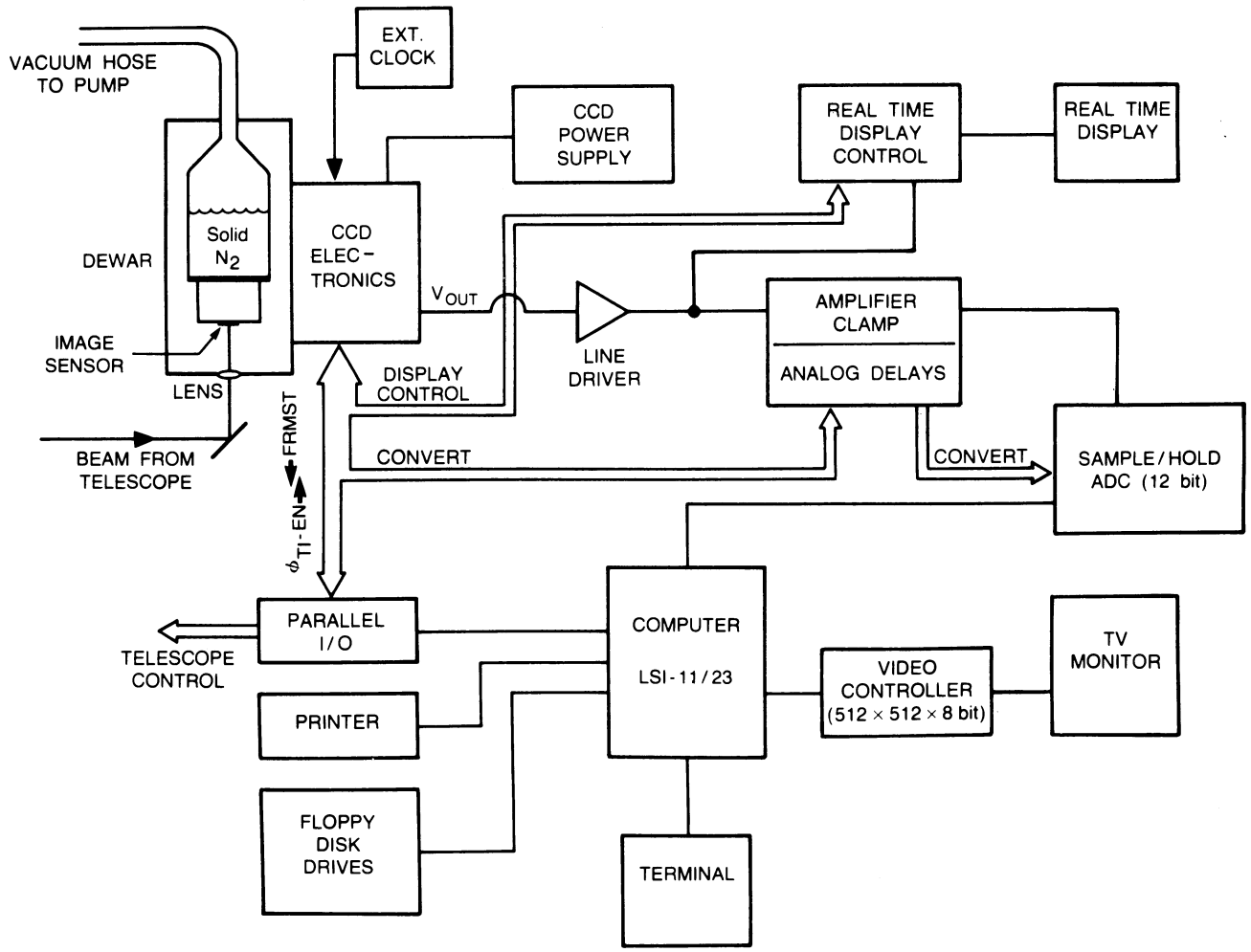

FIG. 1—Block diagram of entire array camera system.

InSb p-n junctions. Although they are all electrically tied together, they can be adjusted to prevent charge from leaking around the junction edges. With proper adjustment of these gates a uniform detector bias and high detector resistance are achieved. "Flashing" (Gillett, Dereniak, and Joyce 1977) is not required with this array as it is effectively replaced by adjustment of the detector gates.

2. The ϕ_{T1} transfer gates allow for essentially 100% duty cycle by separating charge integration from charge readout. They effectively act as a solid-state camera shutter.

3. All shift registers have provision for "fat zero" input, if desired (see Fig. 2a). The fat zero is charge which is electrically inserted into the shift register wells in order to fill the Fast Interface States (FIS, see Sequin and Tompsett 1975), and to increase the charge transfer efficiency (CTE).

4. All shift registers are 64 bits long of which every other bit is used for carrying signal charge. The intervening isolation bits insure nearly zero crosstalk between detectors.

5. Surface channel CCD technology allows low-temperature operation (down to 40 K) and large bucket sizes. The low temperature is necessary to minimize the dark current (see below), and the large bucket size is necessary because of the large background present at wavelengths longer than about 3 μm.

6. The on-chip output amplifier is particularly welcome: by being physically close to the end of the output shift register its input capacitance is very low (about 0.41 $\pm$ 0.04 pF, data supplied by SBRC) thus yielding large charge-to-voltage conversion. The amplifier is configured as a source follower in which the load is a second MOSFET (see Fig. 2b), and the gate of the second MOSFET, V_G can be adjusted to provide variable gain. At our nominal gain setting (about 0.9), a full bucket of 10^7 electrons will result in a signal pulse of about 3 V.

The array is presently housed in a LN_2/LHe dewar. Two optical configurations have been used, and they are shown in Figure 3. In the first configuration, the transfer lens and the 2-mm cold Lyot stop are removed, an $f/8$

cold baffle is placed near the window, and the array is placed at the focal plane of the telescope for direct imaging. In the second configuration the telescope focal plane is reimaged onto the array by a KRS-5 relay lens. At the same time, the telescope secondary is imaged on the Lyot stop, thereby eliminating any extraneous background flux. The dewar also contains a filter slide with five broad-band IR filters (see Table II for filter specifications), as well as a series of light baffles which are all painted with 3M Nextel flat black paint in order to minimize contamination by any stray radiation.

A special fan-out board was built to hold the socket for the 68-pin leadless carrier, on which SBRC had mounted and wired the array, and to provide 1 MOhm static-protective resistors to silicon substrate on all MOS gates. In addition there are 10 kOhm current limiting resistors on all input diffusions.

The electronics needed to operate the array are mounted in a compact box which is strapped piggy-back on the dewar during observations. The electronics include a waveform generator, built by Cayuga Microcomputer Services (Ithaca, NY), clock drivers, bias supplies, and a buffer amplifier, all of which were built in-house.

The output of the array goes to a buffer amplifier/line driver and an external amplifier before reaching the Data Translation DT-2782 12 bit analog-to-digital converter (ADC). The external amplifier has a fixed gain of about 6.7, a variable offset, and a clamp circuit. The circuit clamps on the CCD baseline before each pulse from a detector thereby removing any noise from baseline shifts. This provides the DC stability necessary for long time integrations, and it is similar to the correlated double sampling technique. Finally the digitized signal is stored in computer memory using direct memory access (DMA).

The complete camera system is controlled by an LSI-11/23 computer. All software is written either in FORTH or in assembler. A description of the detector control follows. While the CCD shift registers are run continuously, charge from the V_{ST} storage sites will be dumped into the shift registers only if the ϕ_{T1}-EN line is held high (see Fig. 1). Following such a "charge dump" (CD) the ADC is enabled, and the data are digitized and stored in computer memory. The ϕ_{T1}-EN line is managed by the computer based on our parameter *NF* (Number of Frames per charge dump) and on a TTL pulse from the CCD electronics (FRMST) which interrupts the computer once per frame. If desired, many CDs can be coadded in memory in a double precision buffer in real time before the result is permanently stored on floppy disk. The number of CDs accumulated is determined by the parameter *NCD*. Thus there are two methods of accumulating data: varying *NF* varies the "on-chip" or "hardware" integration time, while varying *NCD* varies the "off-chip" or "software" integration time. How the parameters *NF* and *NCD* are determined will be discussed below. In the present version of the Rochester array camera, the fastest "on-chip" integration employed is 22 msec.

The computer also performs preliminary image processing and controls a 512 × 512 × 8 bit video board (Peritek VCH-Q) which is used to view the acquired images on a video monitor in near real time. A separate real-time display which is independent of the computer (see Fig. 1), built in-house, is used to display the image of bright infrared sources directly on a Tektronix 2215 oscilloscope; this device is invaluable for focusing, dewar alignment, etc.

III. Laboratory Testing

A comprehensive series of laboratory tests have been performed on the array that we have available currently. The tests were designed to determine basic array characteristics, such as quantum efficiency, bucket capacity, charge transfer efficiency, noise, and also other properties more directly related to astronomical work, such as imaging properties under different kinds of operating conditions. The equipment used for laboratory testing is the same as is used for astronomical observations. In describing the tests, reference will be made to Figure 2.

A. *Detector Quantum Efficiency*

Three steps were needed to measure the detector quantum efficiency (*QE*). First the gain of the output amplifier was measured by turning off V_{SCR1}, and by turning on V_{SCR2} and ϕ_R (Fig. 2b). Since the V_{SCR2}/ϕ_R pair then acts as a conducting channel, the potential applied to the V_R diffusion will appear on the amplifier gate. The amplifier gain is given by the slope of V_{OUT} vs. V_R. Gains in the range of 0.53 to 0.9 are selectable by adjusting V_G, the gate of the second MOSFET. The output voltage range is 1.7 V–3.0 V for full buckets, depending on the gain selected. The correspondence between output voltage and input charge is determined using the known gate capacitance of 0.41 ± 0.04 pF. Finally the *QE* is determined by allowing the array to stare at a black surface of uniform, known, temperature. The photon flux incident on the detector is determined using the known filter characteristics, detector area, and solid angle subtended, and the *QE* is calculated. The result is *QE* = 0.60–0.65 for wavelengths between 3.8 μm and 4.7 μm.

B. *Well Capacity*

By proceeding as above, but flooding the array with photons, a well capacity of 10^7 electrons was measured.

C. *Charge Transfer Efficiency*

When looking at a uniformly illuminated scene, we note a small (10% maximum) loss in signal between the

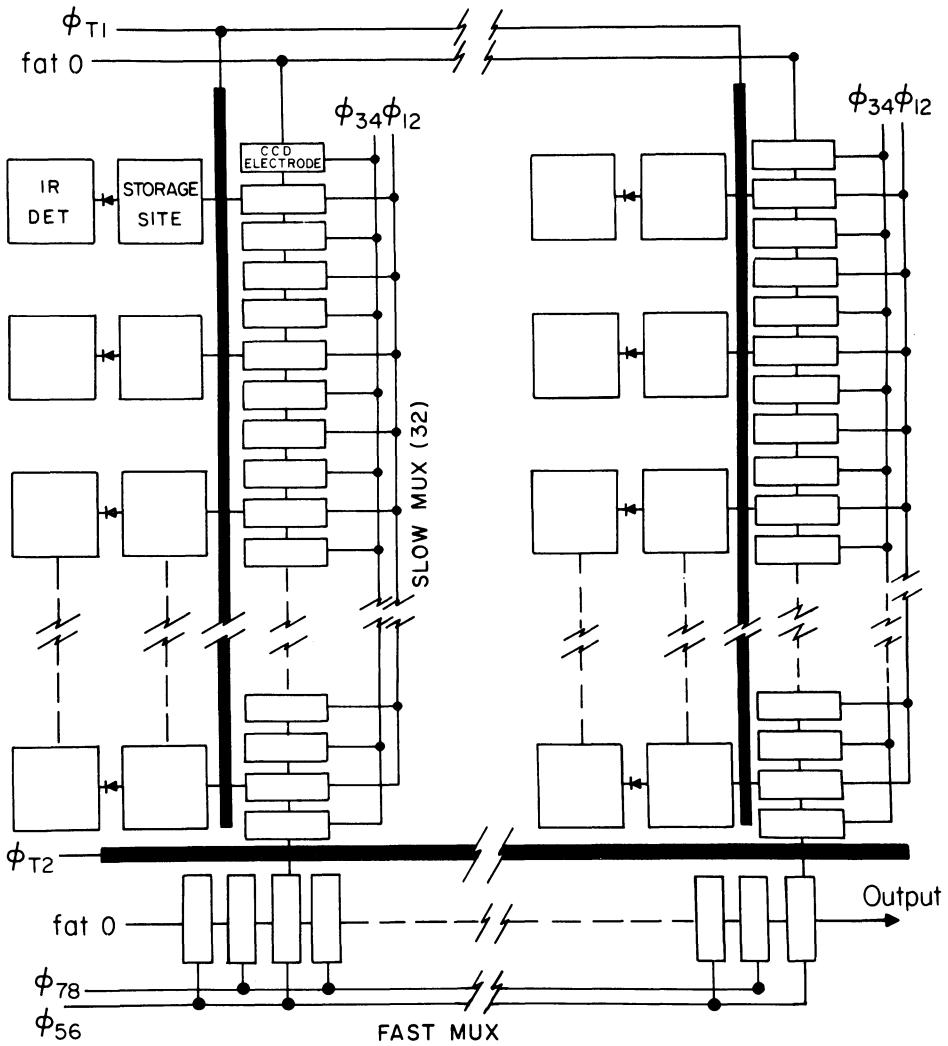

FIG. 2(a)—Simplified schematic of the read-out CCD showing also the connections to the InSb array.

Table I
ARRAY CHARACTERISTICS

Detector material	InSb
Pixel size	90 μm squares on 100 μm centers
CCD well capacity	10^7 electrons
Read-out noise	< 1400 electrons RMS
Full-bucket noise	~ 3900 electrons RMS
Quantum efficiency	60% for $\lambda = 3.8$–$4.7\ \mu$m
Max. read-out rate	100 Hz
No. of working pixels	924 (at high background)
Responsivity uniformity	< 10% deviation from the mean

first detector read out (5 charge transfers) and the last detector read out (253 charge transfers, see Fig. 2a). Some of this degradation could be due to inefficiency of charge transfer, though some of it could also result from imperfect optics (e.g., vignetting of detectors at the peripheries). This gives a lower limit on the charge transfer efficiency which is consistent with that measured by the SBRC (Parrish et al. 1978), and is entirely adequate for good quality imaging.

D. *Dark Current and Detector Resistances*

Dark current and detector resistance are quite important as they determine the ultimate detector sensitivity. These parameters are also related since the dark current is given by $I = V/R$, where V is the actual detector back-bias (10 mV–80 mV), and R is the detector resistance. Tests indicate that the dark current increases by about a factor of 2 for every 2 K increase in detector temperature over the temperature range of 59 K to 69 K. The minimum stable detector temperature we can achieve with our present solid nitrogen dewar is around 60 K. At this temperature, looking at the cold dark slide, a typical detector resistance of 10^{13} Ohms and dark current of 10 fA are achieved.

E. *Detector Uniformity*

The pixel sensitivity uniformity was determined by allowing the array to stare at a uniform-temperature black surface. The sensitivity uniformity is quite good; the sensitivity of any of the working pixels differs by less than 10% from the average sensitivity. The dark current is less

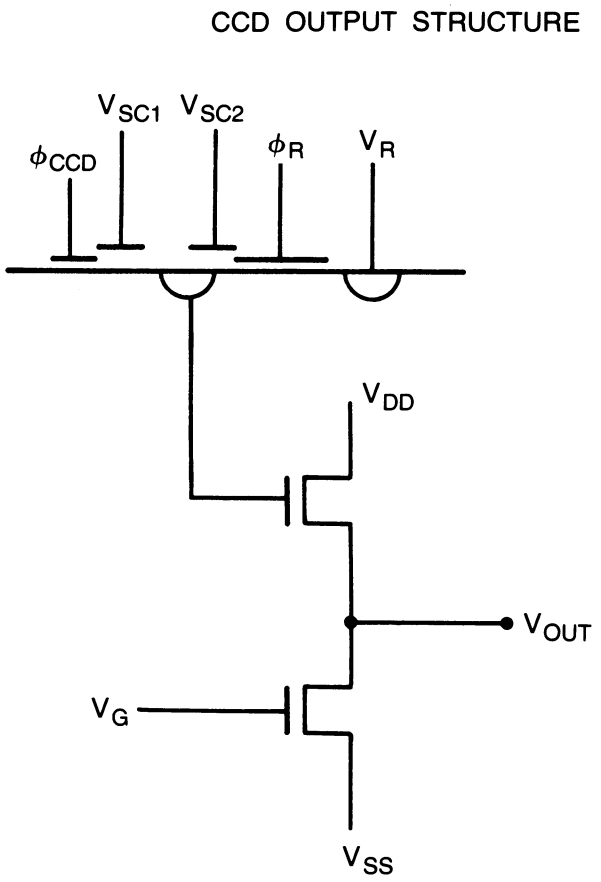

FIG. 2(b)—Detailed structure of the output amplifier. ϕ_{CCD} represents the last CCD gate on the "FAST MUX" of Figure 2(a).

uniform, mostly due to variations of about 70 mV in the zero bias point. Both the effects caused by differing pixel sensitivities and dark current are removed from our images by appropriate image processing (see section IV).

F. *Charge Injection Efficiency*

One criticism of the direct-injection scheme in infrared CCDs has been the possibility of charge injection inefficiency at low backgrounds. In practice we have found that with our device there is always sufficient dark current to assure good charge injection efficiency at our typical operating bias voltage. This can be seen from the following: the small-signal charge injection efficiency at low frequencies, η_{inj}, is given by

$$\eta_{inj} = \frac{g_m R_d}{g_m R_d + 1} \quad ,$$

where R_d is the detector resistance and $g_m = eI/kT$ is the transconductance of the input MOSFET, and I is the MOSFET current (Ando 1978; Bluzer and Stehlik 1978; Longo et al. 1978). For good charge injection efficiency ($\eta_{inj} > 0.67$), we require $g_m R_d > 2$; at $T = 60$ K this corresponds to $I R_d > 10$ mV. In the worst case of negligible photocurrent, I will be provided by the dark cur-

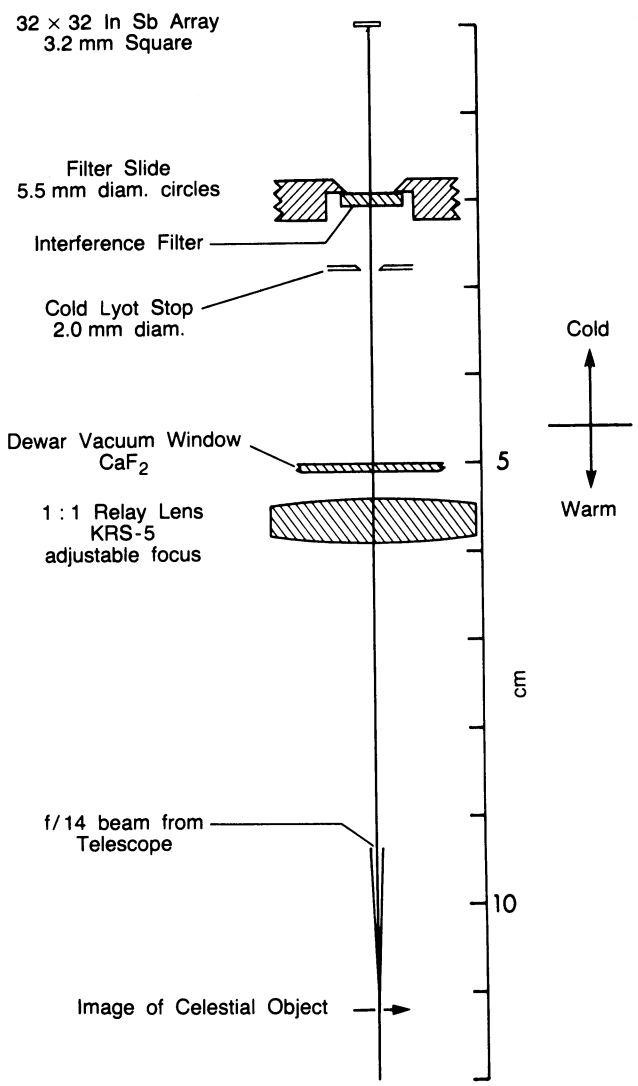

FIG. 3—Optical configuration: The bi-convex KRS-5 lens reimages the focal plane of the telescope onto the detector array while also imaging the telescope secondary onto the cold Lyot stop. Geometrical aberrations have been calculated to be less than 50 μm over the whole array.

Table II

FILTER CHARACTERISTICS

Filt.	λ^*	$\Delta\lambda^*$	Trsm'n
J	1.23	0.23	0.59
H	1.65	0.32	0.77
K	2.23	0.41	0.86
L'	3.75	0.81	0.89
M'	4.67	0.18	0.89
CaF_2	window		0.93
KRS-5	lens		0.7

* In μm.

rent only, and therefore a minimum back-bias of 10 mV is required. The typical minimum amount of back-bias we use when observing is 20mV–30 mV, and we achieve very good images and quite reasonable photometry.

G. *Noise*

We have measured the noise of the CCD under a variety of background conditions and of on-chip integrations times. Our technique is to use a software "pixel-picking" routine to sample a given pixel or sequential set of pixels during several consecutive charge dumps. The data are then analyzed and the average signal and rms (root-mean-square) noise are determined for the pixels under consideration. The results for short and long integration times will be considered separately.

In the laboratory, the high thermal signal with our L' and M' filter and an $f/8$ field of view limits us to short integration times (i.e., 22 msec with $NF = 1$). Under these conditions the rms noise is comparable, but somewhat higher than the shot noise. As the background is reduced, there is excess noise, i.e., the noise level remains constant until, at a fairly low threshold, it begins to diminish approximately as the square root of the background. This behavior is illustrated in Figure 4. It can be seen that near full buckets the noise level is about 1.5 $N^{1/2}$, where N is the total number of holes stored, and that it is considerably higher than this at lower signal levels. At zero background (i.e., with the cold dark slide) the noise level is indistinguishable from our electronic noise floor (0.55 ADU or ADC Units) which corresponds to 1400 noise electrons. We conclude that the actual readout noise of the CCD is less than about 1400 electrons rms. Because of the excess noise at intermediate background as outlined above, however, the best signal-to-noise ratio is achieved when the on-chip integration time (i.e., NF) is set so that the buckets are between half full and full, so that we operate near the $N^{1/2}$ limit.

The source of the excess noise is not completely understood, but it appears to be related to the transfer of charge from the detector storage sites to the SLOW MUX. Looking at the CCD output on an oscilloscope, it can be seen that in addition to a random noise component, a whole frame of output jumps up or down occasionally. By frequency analysis of the signals, Dimmler (1983) has shown that these jumps are correlated in the sense that a jump upward tends to be followed by a compensating jump downward at the next charge dump. Also, the jumps were shown to be positively correlated among the pixels. For the latter reason, this excess noise will not contribute to the pixel-to-pixel noise in an image.

Long integration times at low backgrounds can provide the highest detector sensitivity so the noise here is very important. Our technique is to insert the cold dark slide, to increase NF until the buckets are nearly full, and then to proceed as above. A sample of data is presented in Figure 5 for two pixels in row 20. From Figure 5 it can be seen that there is a large, steady drift in the dark current with time, due to the cooling down of the detector, with a relatively small random noise component superimposed on it. Analysis of the random noise component yields an rms noise of 3900 electrons with buckets near half full, and with a 44 sec integration time. Thus, the noise performance is about the same at both high and low backgrounds (22 msec to 44 sec) for half-full buckets.

H. *Detector NEP*

For an integrating detector with quantum efficiency QE and an rms noise ΔN in an integration time t, the de-

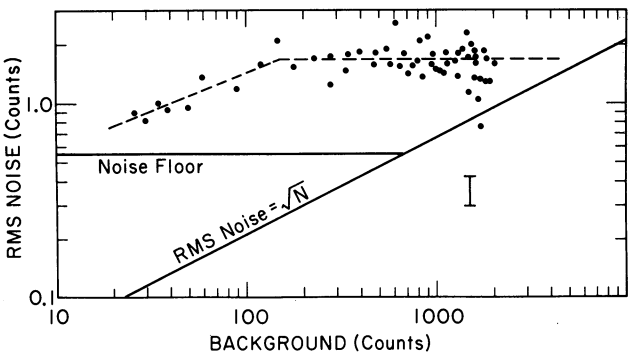

FIG. 4—Detector noise as a function of 4.7 μm background. The dots are the measured values, and the I-beam represents the typical measurement error. The noise floor is the lowest noise that we can measure using our current experimental setup: it represents the ADC digitization noise. The line labeled "RMS noises = $\sqrt{N}$" represents the best possible detector performance due to shot noise in the background. One count represents about 2500 electrons and full buckets give 4000 counts.

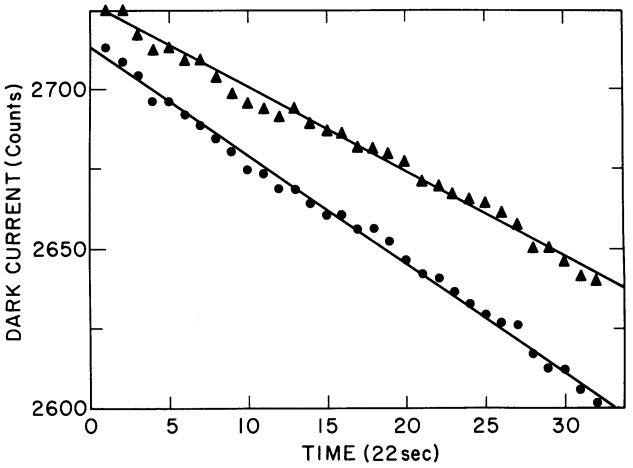

FIG. 5—Dark current as a function of time of two individual detectors with a 22-sec on-chip integration time. One count (= 1 ADU) corresponds to about 2500 electrons. The steady decrease in the dark current is due to the steady decrease in detector temperature. The small variations around the solid line were used to determine the detector noise at low backgrounds (long integration times).

tector *NEP* will be given by

$$NEP = \frac{\sqrt{2}\,\Delta N\, h\nu}{QE\,\sqrt{t}} \quad ,$$

where $h\nu$ is the photon energy. Using our measured QE at 3.8 μm, noise ΔN, and using $t = 22$ msec appropriate for high background operations, the $NEP = 4 \times 10^{-15}$ W Hz$^{-1/2}$ which is about a factor of two above the BLIP (Background Limited Performance, $QE = 1$) limit. At low background we are limited by dark current rather than by background photons. For an integration time (at 60 K) of 44 sec, the longest for which we have an extensive set of laboratory noise data, the $NEP = 9 \times 10^{-17}$ W Hz$^{-1/2}$ at 3.8 μm. At a temperature of 50 K we anticipate that 1000 sec or longer integration times would be possible, and an $NEP = 2 \times 10^{-17}$ W Hz$^{-1/2}$ or better could be achieved. In fact we have achieved integration times of 240 sec at the telescope at lower temperatures (see section IV.A).

IV. Astronomical Imaging and Image Processing

Our techniques of astronomical imaging and of image processing are described below. These techniques were developed to allow us to remove the contribution of the background, be it sky emission or dark current, from our images, to compensate for the variable pixel sensitivity and nonuniform illumination, to remove the effects of the bad pixels, to calibrate the flux levels of the scenes imaged, and to combine several images in order to provide the full image resolution.

A. *Observing Technique*

In order to compensate for the effects of variable pixel sensitivity and nonuniform illumination of the array, a flat field is observed. The ideal flat field is an object of uniform surface brightness, located at infinity, and slightly larger than the whole CCD. The closest approximation to this that we have found is the moon. We know that, in fact, much of the moon is not flat in the infrared, but we have found that there are positions in large maria, near the subsolar point, which are adequate for our purposes. In addition, in order to increase the flatness of the field, we defocus the telescope during the observation. The signal from the moon is determined by subtracting a background frame taken of the nearby sky from the moon frame pointed at the mare of choice. We are also investigating the possible use of the daytime sky at *J*, *H*, or *K* to determine the flat field.

To calibrate the flux levels of our images, we observe relatively bright stars through the night. At each wavelength the star is imaged at four or more positions on the detector. By then subtracting two of the images, a positive and a negative star image are produced without the need for separate sky observations. The images are flattened, and all pixels which have signal are summed to give the total star signal. From the known star brightness, the counts for zero magnitude (*CFZM*) are then calculated. The *CFZM* are later used to calibrate other images. This technique also allows us to check the flatness of the field.

For each observation of an astronomical object, a decision must be made as to the on-chip and the off-chip integration time. Because of our detector noise properties, the best signal-to-noise ratio is achieved when the on-chip integration time (hereafter T_0) is the maximum consistent with not overfilling the buckets. On the other hand, the dynamic range in each frame is limited by the amount of background charge present, which increases linearly with the on-chip integration time. Therefore a compromise between dynamic range (low T_0) and sensitivity (high T_0) must be made. The compromise chosen depends on the source being observed. Thus the total integration time $T = NCD \times T_0$, where *NCD* is the number of frames coadded in software, and *NCD* is chosen given T and the largest possible T_0, consistent with adequate dynamic range and stability of the background.

For low background observations, i.e., with the *J*, *H*, and *K* filters, T_0 is limited by the thermal dark current. With solid nitrogen as a cryogen the detector temperature is about 60 K, and we have used T_0 in the range of 24 sec to 95 sec ($NF = 1000$ to 4000). On two occasions we added liquid helium to the cryogen thus decreasing the temperature and reducing the dark current enough to allow $T_0 = 4$ min ($NF = 10{,}000$) while retaining good imaging properties; on these two occasions we were able to detect a sky/telescope background at 2.2 μm of about 5000 e$^+$/sec which was 1/4 of the dark current (1″ square pixels, during a cold winter night on the Kitt Peak National Observatory 1.3-m telescope, which was configured as a low-background telescope).

Through the *L′* and *M′* filters our sensitivity is limited by the high thermal background. At these high backgrounds we have used T_0 in the range of 100 to 500 msec depending on the optical configuration used and on the outside atmospheric temperature.

The total integration time, T, is chosen on the basis of the source being observed and on the wavelength of the observation. At long wavelengths, because of the relatively rapid variations in sky emission, we have limited T to 90 sec or less, with $T = 24$ sec more typical. At the shorter wavelengths we are limited by drifts in the dark current, but this is well behaved, and integration times as long as 3 min are routinely used with no problem. In either case, several observations of a source are usually obtained and combined later.

Four components make up the total signal observed in an individual scan: electrical offset, sky background, dark current, and source signal. The last component is generally the one of interest, and it is usually also the

smallest one. Our observing procedure is to take scans in the sequence sky-source-source-sky. The sky signals are later used to subtract the unwanted components from the total signal to yield the source signal.

To obtain the maximum spatial information about the regions of interest, each scene must be imaged four times per resolution element (i.e., Nyquist sampling) provided that we are not diffraction limited. The four source positions (S1–S4) are chosen, and the background sky position (BG) is chosen to be 100″ to 300″ away, at a position where no celestial objects appear in the field. Thus a complete sequence at one filter consists of: BG0-S1-S1′-BG1-S2-S2′-BG2-S3-S3′-BG3-S4-S4′-BG4. Adjacent backgrounds are used for each source frame (i.e., BG0 and BG1 for S1 and S1′, BG1 and BG2 for S2 and S2′, etc.). The source positions S1–S4 are partly to satisfy Nyquist sampling and partly to minimize the effects of the bad pixels (see below). The multiple source scans also add redundancy to the data and are helpful in identifying the noisy pixels.

B. *Image Processing*

Since the output of the CCD is not precisely linear, the first step in our image processing is to compensate for this nonlinearity. This effect has been calibrated, and we find that near full buckets the gain decreases slightly. The maximum error is about 14%. Linearization of the raw counts consists of multiplying them by a factor between 1.00 and 1.14 depending on signal amplitude. The major effect of this step is to improve our calibration accuracy.

The next process is to subtract the background from the object frames. By taking an appropriate linear combination of the sky frames obtained just before and just after the source frames, good sky subtraction can be obtained over the whole CCD. After this step the result is divided by a flat field in order to compensate for the variable pixel sensitivity. At this point the processed images are examined; images in which sky subtraction did not result in a flat sky and images with other possible defects are rejected, and the remaining frames are processed further.

For the remainder of the image processing, one frame is designated as the "master" frame; the master is selected on the basis of position of the source on the array, flatness of the sky, sharpness of the image, etc. The remaining frames are designated as "slave" frames. The next two steps involve replacing the data in the bad pixels of the master frame with good data from the shifted slave frames, and coadding shifted the slaves into an expanded master in order to obtain the full resolution. Before the next two steps can be performed, the offsets between the master and the slaves must be determined, and a list of bad pixels must be generated.

The offsets between the master and the slaves are determined by shifting the slaves and blinking them (as in a blink comparator) with the master. Different offsets are tried until the justification is deemed accurate. The offsets can typically be determined to an accuracy of a few tenths of a pixel using this technique. Another technique which has been used consists of determining the centroid of the light distribution from a source seen on both the master and the slave frames. The difference in the centroid positions gives the relative shift. This technique only works well when a bright point-like source is present, and the offsets determined in this way are always checked by blinking. Blinking alone is used under less favorable circumstances.

Our best array has 97 pixels which are not sensitive to infrared radiation (dead pixels), a few pixels with excess noise, and up to 50 more (depending on chip temperature and integration time) with excess dark current (leaky pixels). To determine the signal at the positions of these bad (= dead + noisy + leaky) pixels, we use multiple frames in which the object is imaged at different positions on the CCD. Since we must take a minimum of four source frames to satisfy the Nyquist sampling theorem, we choose the spacing so that bad pixels in one frame are covered in one or more of the other frames. In a typical sequence of four frames we can usually replace 75% of the bad pixels in the master frame with good data. The remaining bad pixels are finally "fixed" by replacing them with a mean of adjacent good pixels. Before, and sometimes during, each night's observing, a series of frames are taken at high and low backgrounds which allow us to identify the dead, noisy, and leaky pixels. The lists are used to guide our data reduction.

Once the bad pixels in the master frame have been replaced or fixed, that frame is expanded into a 63 × 63 array by placing each pixel of the master into every other pixel of every other row of the large array, and by interpolating linearly in order to assign values to the intervening pixels. The slave frames are then added to the big array after expanding them and shifting them. Data at the positions of the bad pixels in the slave frames are flagged and are not used. The final images are displayed with four (2 × 2) pixels per resolution element, and with minimal degradation in resolution.

V. Astronomical Images and System Performance

A. *Images*

We now present some of the images obtained with the imaging camera. A list of the images is presented in Table III, the integration times include both source and sky observations. For the images displayed in Figures 6–12 North is up and East is to the left. For the Mees data, the images are 80″ across (2.5 square arc-sec pixels) while for the KPNO data the images are 32″ across (1 square arc-sec pixels). A short description of the images

are given in the figure captions; more detail will be given in research papers that are currently in preparation.

Table III
TECHNICAL DATA ON IMAGES

Fig.	Source	Filt.	Tel.	T*	UT Date	Max. Sig.†
6.a	Jupiter	*H*	Mees	10	26-Mar-83	87
6.b		*K*	Mees	60		1.9
6.c		*M'*	Mees	35		156
7.a	Saturn	*H*	Mees	14	25-May-83	42
7.b		*K*	Mees	14		2.6
7.c		*L'*	Mees	134		0.53
8.a,b,c	Orion BN-KL	*K*	Mees	198	1-Nov-83	1.6
9.a,b		*K*	KPNO	425	22-Jan-84	0.6
10.a	OH 0739 — 14	*H*	KPNO	1135	28-Jan-84	0.08
10.b		*K*	KPNO	1636		0.12
10.c		*L'*	KPNO	293		2.4
10.d		*M'*	KPNO	212		7.4
11.a,b	M82	*H*	Mees	651	, #	0.065
11.c,d		*K*	Mees	423	#	0.092
12.a		*H*	KPNO	1514	25-Jan-84	0.019
12.b		*K*	KPNO	2649		0.025
12.c		*L'*	KPNO	284		0.02

* Total observing time required for image in seconds.
† in Jy per pixel; pixel sizes: Mees: 2″5; KPNO: 1″0.
# Data from 24-Mar and 28-Apr-83.

B. *System Performance*

The system sensitivity has been determined from data gathered during our January 1984 run on the KPNO 1.3-m telescope. Frames in which there is a clearly observed source were calibrated to units of flux density per pixel. A typical portion of the frame where no obvious sources were located was analyzed; the RMS fluctuations in this part of the frame were taken to be the 1 sigma noise level. On a typical image, the contour at the 5- to 6-sigma level is quite well defined, easy to draw by hand, and represents "clearly observed" emission. The resulting sensitivity for a typical 1″ square pixel (2.2×10^{-11} ster) is presented in Table IV. At L' and M' we are background limited while at J, H, and K we are dark-current limited. The dynamic range (max signal/3-sigma noise) is about 4500 at L' and 800 at K for the frames analyzed above, using a fixed on-chip integration time. Dimmer sources can be detected by increasing the observing time.

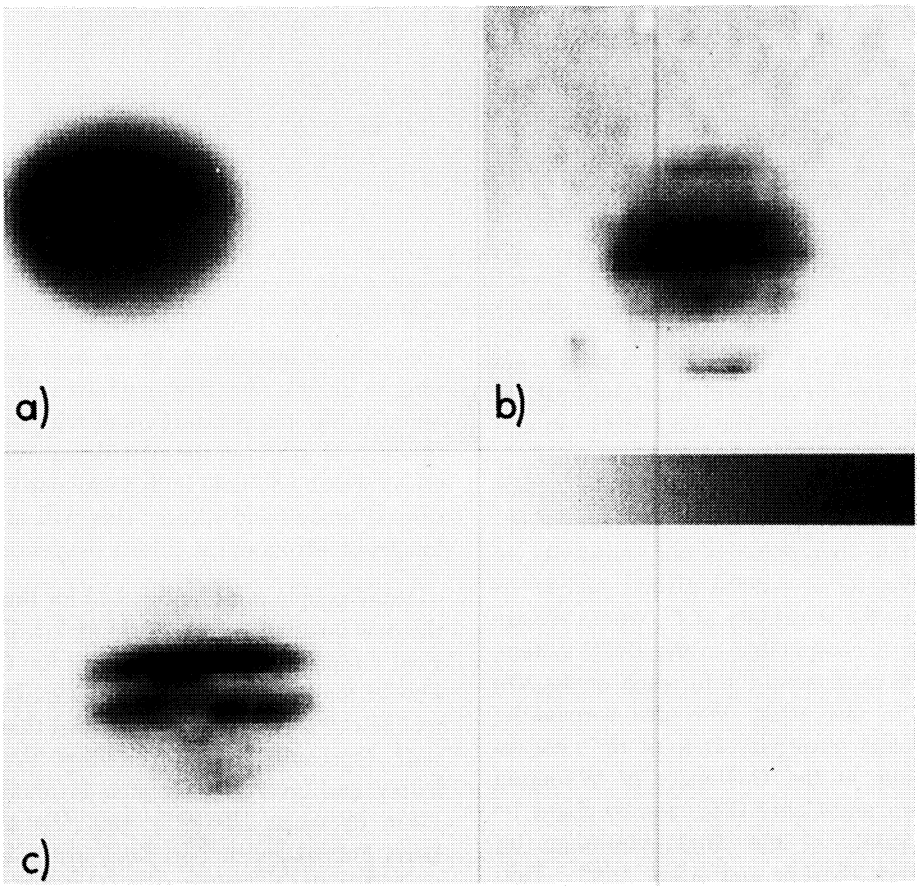

FIG. 6—Jupiter at 1.65 μm (*H*), 2.23 μm (*K*), and 4.67 μm (*M'*), linear display: see Table III for details. The *H* image (top left) is most similar to the visible appearance, with the Zones and the Great Red Spot, just SE of center, appearing slightly brighter. At *M'* (lower left) we are seeing mostly thermal emission from deeper atmospheric levels through an atmospheric window. The emission is concentrated in two bright belts straddling the equator. The peak brightness temperature is about 240 K, and the Great Red Spot is seen as a cooler region there. In the *K* band (top right) the scattered light level is greatly diminished due to the strong molecular absorption in the Jovian atmosphere. The maximum albedo is only about 0.01 and the brighter regions seen are due to high-level haze. Interestingly the Great Red Spot appears as a bright spot here, indicating that a high haze is hovering over this atmospheric structure.

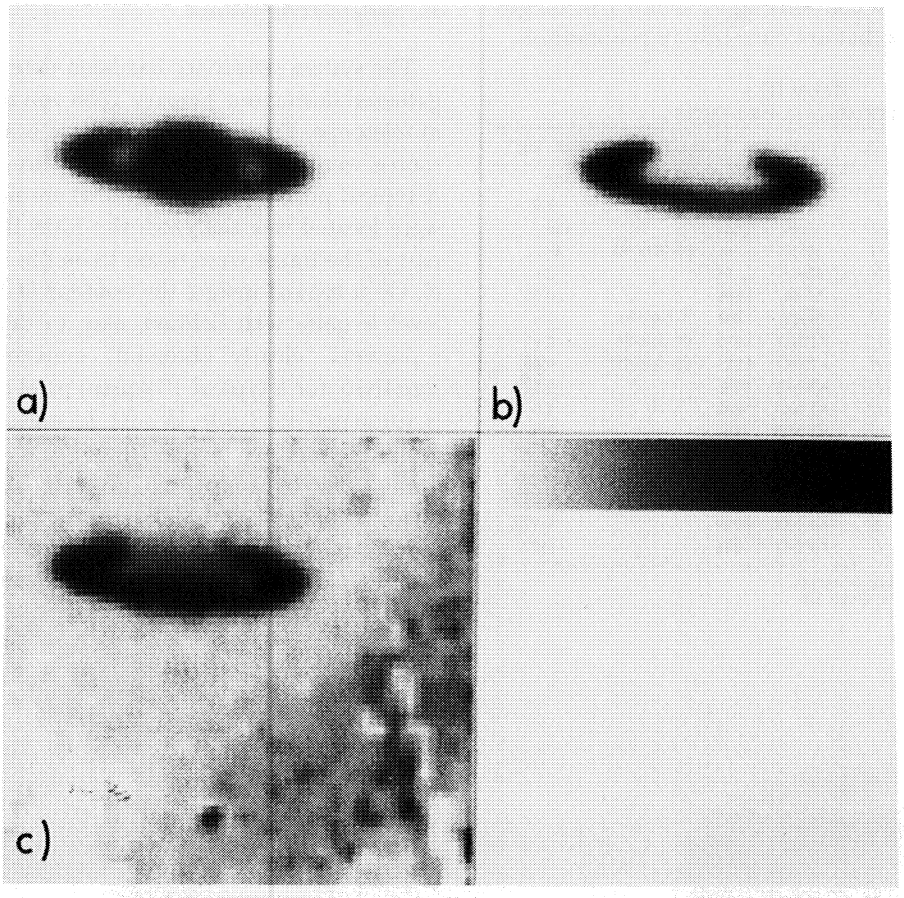

FIG 7—Saturn at H, K, and L', linear display; see Table III for details. At K (top right) the disk of the planet almost disappears due to strong molecular absorption, while the solid rings remain bright. At L' (lower left) the disk is again dimmed by molecular absorption, while the rings are dimmed by water-ice absorption. The flux densities from the brightest parts of the rings are H: 29; K: 16; L': 1.2 Jy per pixel.

The performance levels in Table IV have been compared to the sensitivities for single-element InSb detector systems from the literature. The May 1983 Observer's manual for the Infrared Telescope Facility (IRTF) 3-m telescope quotes a 1-sigma sensitivity of $K = +19\overset{m}{.}8$ and $L' = 15^m$ (6″ circular aperture) in one hour of observing. Appropriately extrapolating our sensitivity to these conditions gives $K = +20\overset{m}{.}6$ pixel^{-1} and $L' = +14\overset{m}{.}8$ pixel^{-1}. Thus the sensitivity at L', where we are background limited, is comparable to the IRTF system, but at K we are $0\overset{m}{.}8$ more sensitive for each of the 870 working detectors in our array. We also surpass by about 1^m the published sensitivity at K of the new integrating InSb system at the University of Wyoming (Hackwell, Grasdalen, and Gehrz 1983) and by about 1^m the published sensitivity of the Anglo-Australian integrating InSb system (Barton and Allen 1980). Thus each of the approximately 900 working pixels on our array performs as well or better than the best single element InSb detector currently in use for astronomy.

VI. Conclusion

We conclude with some prospects for future improvements in the instrument. In the near future we are planning to build a new dewar which will allow us to operate at colder temperatures, and with better temperature stability. In addition the new dewar will contain a filter wheel which will hold both a circular variable filter, and several broad-band filters. This will allow us to obtain images of astronomical objects in spectral lines.

Many people must be thanked for their help in getting the new imaging system working: Dr. Barbara Jones, Dr. Fred Gillett, and Dr. Dick Joyce for the filters, Dr. Al Fowler for some electrical drawings, Dr. Martin Harwit for the dewar. We also give special thanks to the KPNO staff, especially Dick Joyce, Ron Probst, Chuck Mahaffey, and Jay Parks, for their invaluable help with the 1.3-m telescope observing run. We also acknowledge Larry Forsley and Robert Keck of the Laboratory of Laser Energetics for supplying and supporting our FORTH system, Justin Schoenwald for excellent system programming, Pat Borelli for excellent and prompt machining, T. Hayward and D. Kozikowski for assisting during the observations, and W. M. Dimmler and Dr. R. W. Boyd for help in evaluating the detector. One of us (C.E.W.) wishes to acknowledge the Xerox Corporation for partial

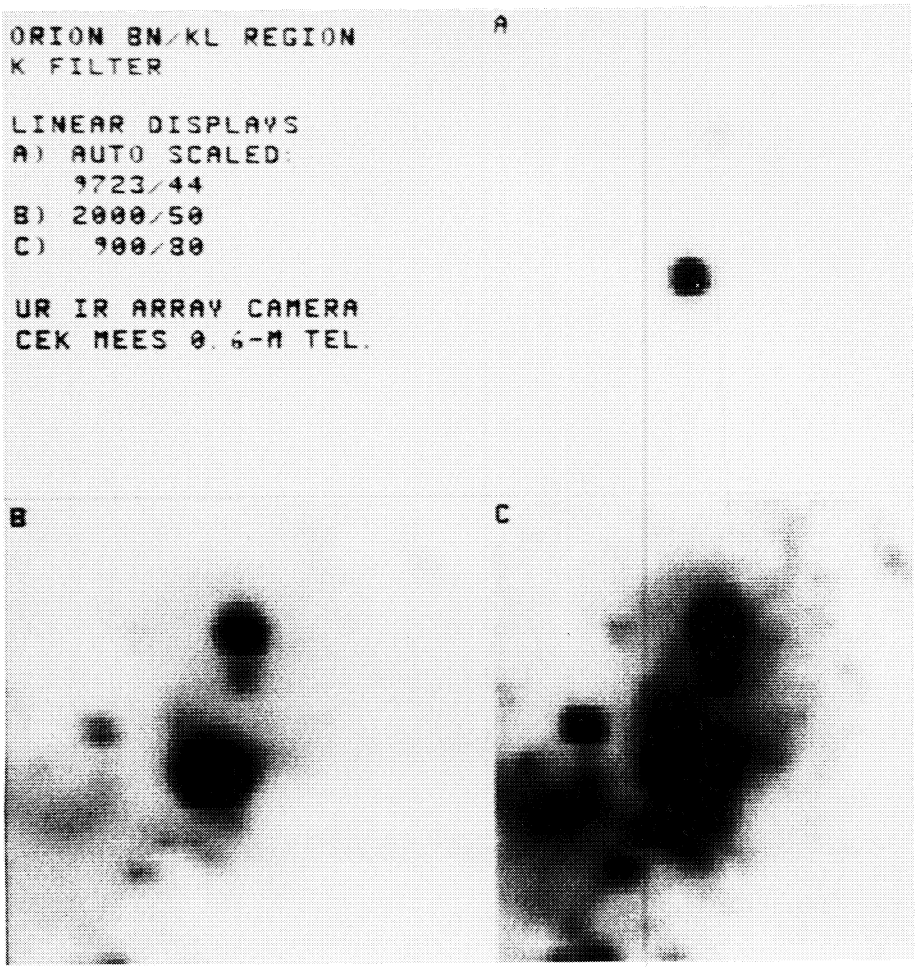

FIG. 8—Orion BN-KL region from Mees at 2.23-μm (K) linear displays; see Table III for details. BN is the brightest source near the center of the picture. Parts B and C display the same data as A emphasizing increasingly lower levels of emission.

support. This research was supported by NASA Ames grant NAG 2-117 and Office of Naval Research, CNA SUB N00014-76-C-0001.

REFERENCES

Ando, K. J. 1978, *NASA-CR-152*, 169.
Barton, J. R., and Allen, D. A. 1980, *Pub. A.S.P.* 92, 368.
Bluzer, N., and Stehlik, R. 1978, *IEEE Trans. on Electron Devices* ED-25, 160, No. 2.
Dimmler, W. M. 1983, M.S. Thesis, The Institute of Optics, University of Rochester.
Forrest, W. J., and Pipher, J. L. 1983, in *Proc. Infrared Detector Technology Workshop*, C. McCreight, ed. (NASA Ames Research Center).
Forrest, W. J., Moneti, A., Woodward, C. E., and Pipher, J. L. 1983, *Bull. A.A.S.* 15, 651.
Gillett, F. C., Dereniak, E. L., and Joyce, R. R. 1977, *Opt. Eng.* 16, 545.
Hackwell, J. A., Grasdalen, G. L., and Gehrz, R. D. 1983, *Bull. A.A.S.* 15, 642.
Hoendervoogt, R. M., Kormos, K. A., Rosebeck, J. P., Toman, J. R., and Burgett, C. B. 1978, in *IEEE International Electron Device Meeting*, p. 510.
Longo, J. T., Cheung, D. J., Andrews, A. M., Wang, C. C., and Tracy, J. M. 1978, *IEEE Trans. on Electron Devices*, ED-25, 213, No. 2.
Moneti, A. 1984, Ph.D. Thesis, University of Rochester.
Moneti, A., Forrest, W. J., Woodwrd, C. E., and Pipher, J. L. 1983, *Bull. A.A.S.* 15, 683.
Parrish, W. J., Renda, F. J., Ray, N. L., Maeding, D. G., Eck, R. E., and Toman, J. R. 1978, in *IEEE International Electron Device Meeting*, p. 513.
Sequin, C. H., and Tompsett, M. F. 1975, *Charge Transfer Devices* (New York: Academic Press), p. 111.

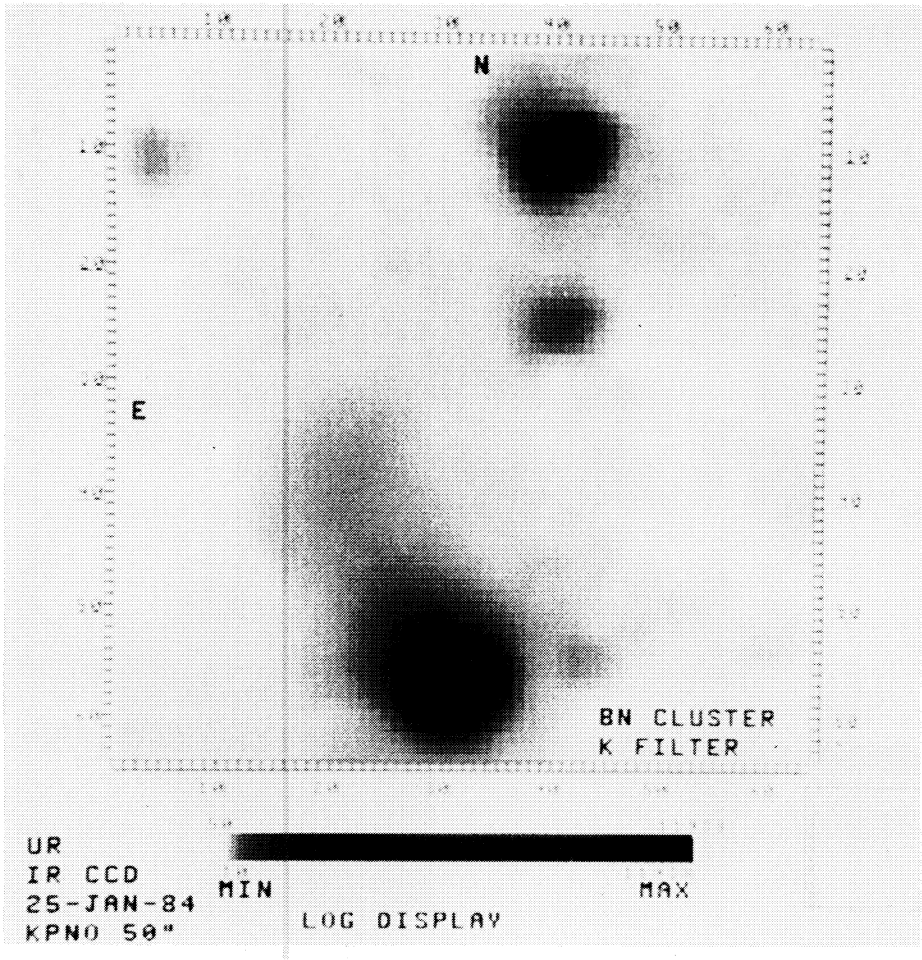

FIG. 9(a)—Two views (log display) of the BN-KL region at *K* from KPNO: (a) the region N of BN including IRc9.

FIG. 9(b)—The region S of BN. Note the smooth jet-like structure emanating from BN toward the NE and curving toward the N. We propose that this jet represents scattering off a disk.

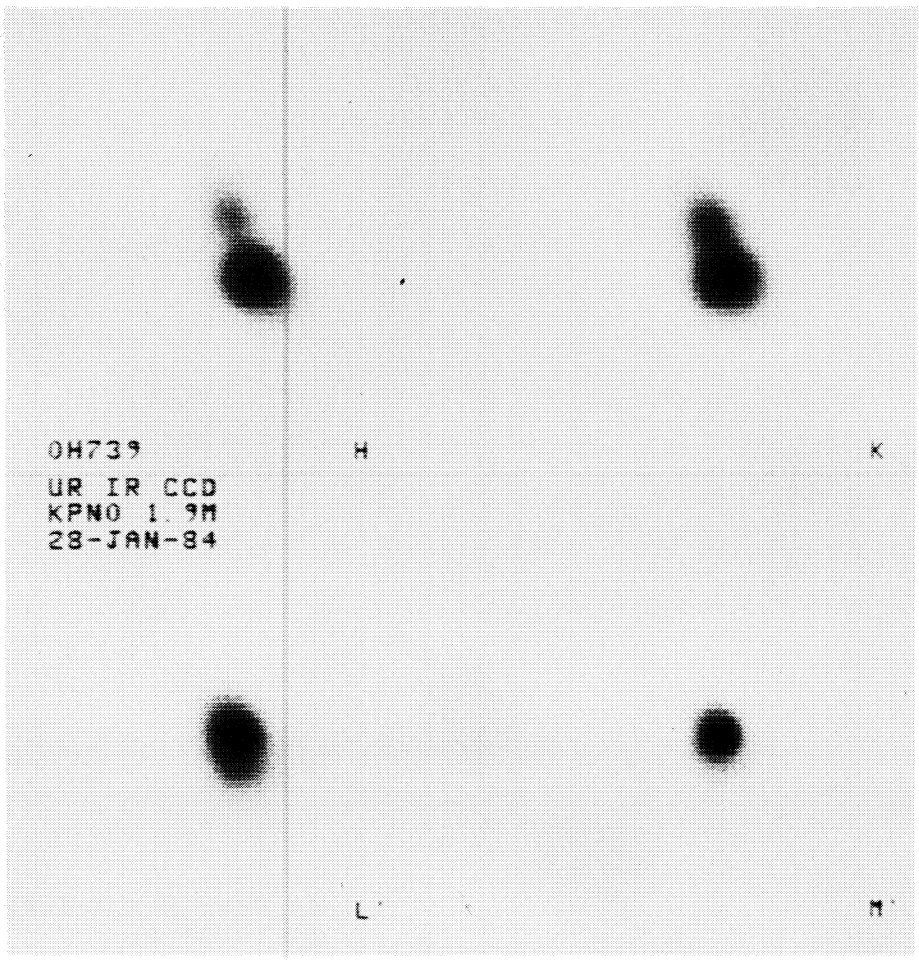

FIG. 10—OH 0739-14 from KPNO, linear display; see Table III for details. This is a bipolar reflection nebula around a late-type star undergoing mass loss. The reflection nebulosity is seen at the short wavelengths (*H* and *K*), whereas at the long wavelengths the central source in the obscuring dust lane becomes dominant.

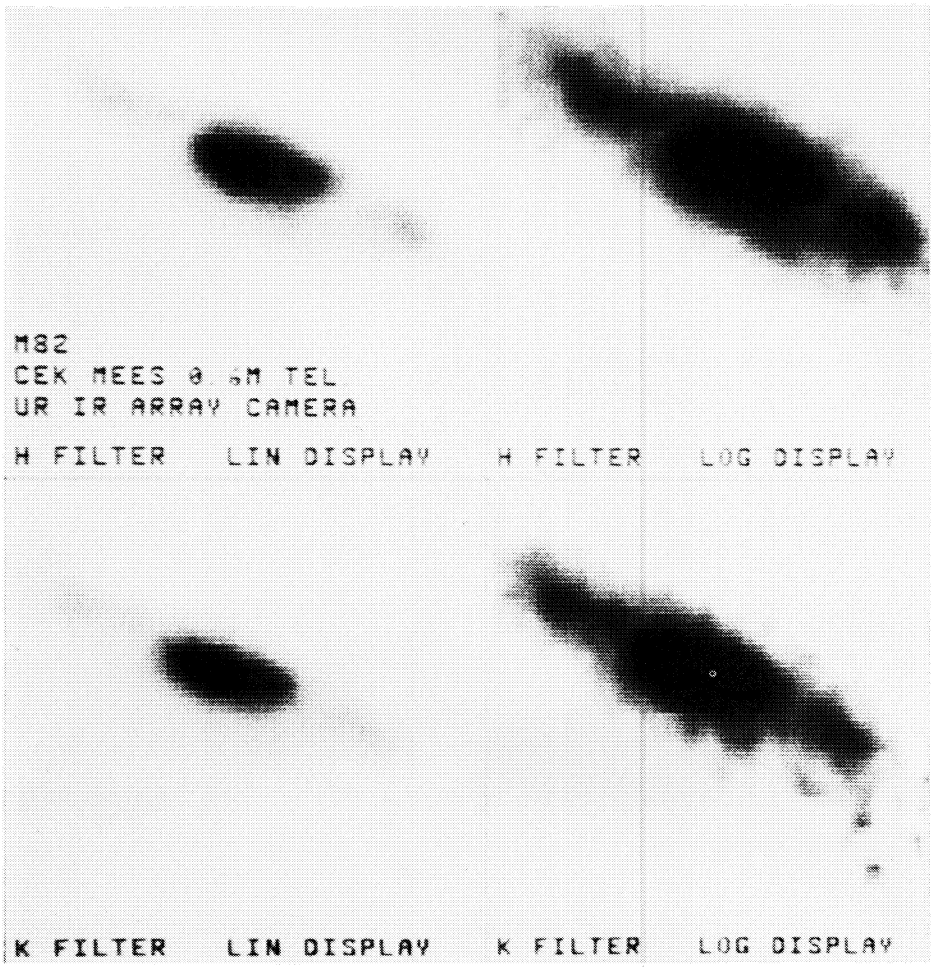

FIG. 11—M82 from Mees at H and K displayed both linearly and logarithmically; see Table III for details. Note the two lobes of emission symmetrically placed above 25″ to each side of the nucleus. These lobes had not been observed before.

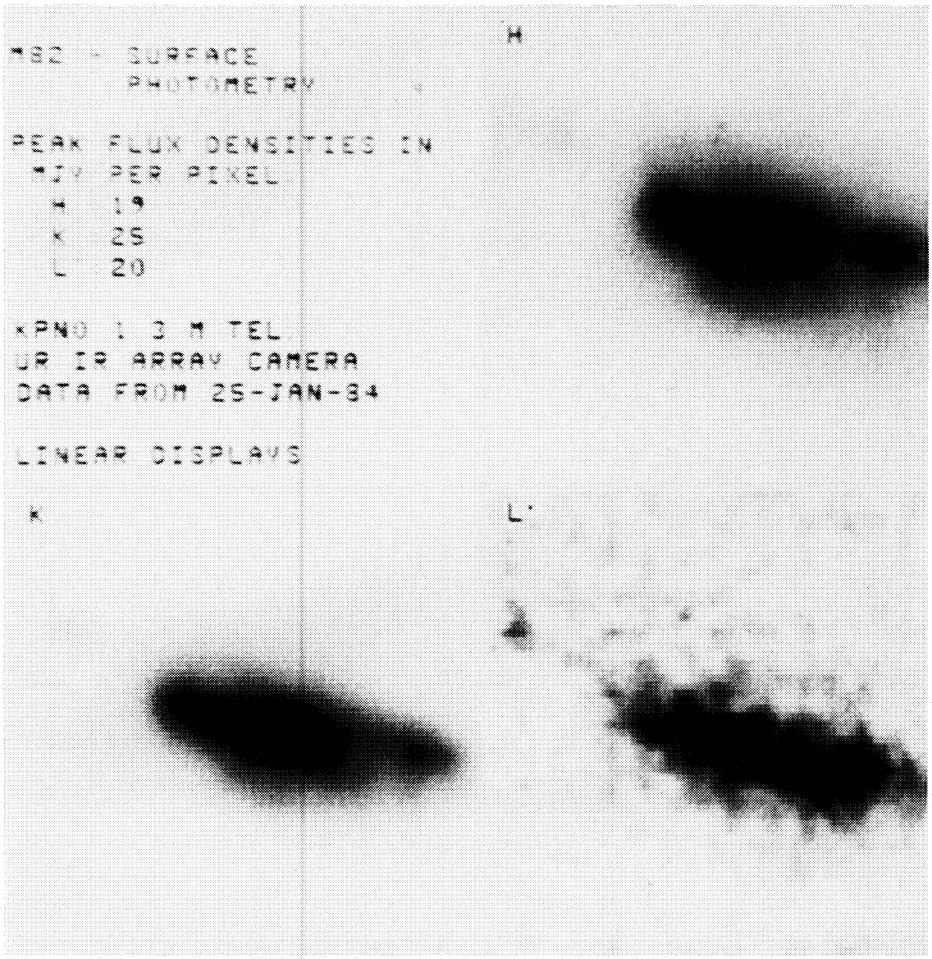

FIG. 12—M82 from KPNO, linear display; see Table III for details. The area imaged in this Figure corresponds to the central regions of Figure 11. Note the point-like source seen about 12″ SW of the nucleus, in the region of the currently most intense star-forming activity. This source is also faintly visible in Figure 11.

Table IV

SYSTEM SENSITIVITY, KPNO 1.3 m

Filt.	T†	1σ Noise/Pixel* mag	Jy	W cm^{-2} μm^{-1}	No. of working pixels
L'.....	27	+13.0	1.6×10^{-3}	3.5×10^{-20}	920
K.....	355	+17.5	64×10^{-6}	3.8×10^{-21}	870

* Pixel size: 1″.0 square.
† Total observing time required for image in seconds.